

Finite-size resource scaling for learning quantum phase transitions with fidelity-based support vector machines

Aaqib Ali ^{1,2,3} Giovanni Scala ^{4,2} Cosmo Lupo ^{4,1,2} and Antonio Mandarino ³

¹*Dipartimento Interateneo di Fisica, Università di Bari, 70126 Bari, Italy*

²*INFN, Sezione di Bari, 70126 Bari, Italy*

³*International Centre for Theory of Quantum Technologies, University of Gdańsk, 80-308 Gdańsk, Poland*

⁴*Dipartimento Interateneo di Fisica, Politecnico di Bari, 70126 Bari, Italy*

Quantum kernels offer a valid procedure for learning quantum phase transitions on quantum processing devices, yet issues on the scalability of the learning strategy in connection with the symmetry of the critical model have not been clarified. We derive a link between model symmetry and fidelity-kernel resource scaling. We quantify the measurement resources required to estimate fidelity-based quantum kernels for many-body ground states while preserving the structure of the resulting Gram matrix under finite-shot sampling. Crucially, we show that increasing symmetry in the underlying spin model systematically amplifies these shot requirements. Moving from the \mathbb{Z}_2 -symmetric Ising/ XY regimes to the $U(1)$ -symmetric XX (and XXZ) regimes leads to stronger kernel concentration and therefore substantially larger shot costs under the same bounds. We consider a tunable one-dimensional spin- $\frac{1}{2}$ Hamiltonian spanning the transverse-field Ising, XY , XX , and XXZ limits, and define the kernel as the ground-state fidelity. Kernel entries are estimated using a SWAP-test estimator with S shots, and we adapt the ensemble spread and concentration-avoidance shot bounds to obtain practical shot requirements in terms of the interquartile range of kernel values and a representative kernel magnitude. For the free-fermion XY/XX family, we use the closed-form Bogoliubov-angle fidelity, while for the interacting XXZ chain we compute fidelities by exact diagonalization and benchmark shot-noise effects. Our symmetry-aware bounds provide a pragmatic procedure for physics-informed quantum machine learning.

I. INTRODUCTION

Spin chains are paradigmatic models in which spin- $\frac{1}{2}$ particles interact along a one-dimensional lattice. Despite their apparent simplicity, they capture a broad range of many-body emerging phenomena, to name a few formation of magnetic domains in materials, generation of multipartite quantum correlations, and even topological order [1–5]. In all these phenomena, *quantum phase transitions* (QPTs) play a crucial role. They are zero-temperature transitions between distinct ground-state phases of a many-body system, driven not by thermal fluctuations but by quantum fluctuations [6–9]. QPTs reveal how quantum fluctuations induce abrupt changes in the structure of the ground state, unveiling universal behaviour and critical phenomena that are fundamental to understanding quantum many-body physics. Although QPTs are strictly defined for $T=0$ phenomena, their signatures have been observed in analog quantum simulation at ultra-low temperatures, typically in the nK regime [10–14]. Despite long research efforts, QPTs are one of the most challenging problems in modern physics, since the scaling of correlations close to the critical points plays a pivotal role in lattice field theories as well as in non-equilibrium processes. As a result, considerable effort has focused on computational approaches to characterize critical points and finite-size scaling. The current effort focuses on utilizing methods rooted in machine learning and data-driven approaches. The unifying concept stems from the common statistical approach of learning strategies and systems exhibiting phase transitions. Instead of modeling all microscopic degrees of

freedom, one can learn a decision rule from data using similarity in an appropriate feature space.

Machine learning (ML) has emerged as a powerful framework for detecting quantum phase transitions (QPTs) across spin systems [15–18]. From convolutional neural networks that recognize spatial patterns in the transverse-field Ising model [19] to unsupervised ClassiFIM that leverages Fisher information geometry [20] and clustering approaches [21–23], various methods now complement the traditional approach that relies on the discovery of order parameters.

A special class of learning strategies is support vector machines, and methods emerged as a natural tool for investigating classical statistical mechanics models [24] and learn the relevant structure by comparing states through a feature map rather than explicitly resolving all degrees of freedom. In particular, we aim to investigate quantum-informed support vector machines that implement the kernel via a quantum feature map, using quantum circuits to evaluate similarities in a feature space that finds its roots in the geometry of the ground states of the systems under investigation. This approach provides a natural bridge between quantum representations and classical maximum-margin classification.

Quantum support vector machines (QSVMs) [25] offer the ability to explore the transitions encoding many-body ground states into feature spaces where kernel evaluations yield quantum-state overlaps [26–28]. We adopt fidelity-based quantum kernels for compelling reasons that recently emerged in the literature. It has been proven that they can offer complexity advantages over classical kernels [29–31], and nowadays experimen-

tal platforms are suitable to realize them [32]. Moreover, theoretical insight on the successful classification of symmetry-protected topological and symmetry-broken phases has been reported in [26, 27], and expanded, taking into account the kernel concentration and sample complexity [33].

In this work we present a pathway to incorporate the quantum digital simulation of critical systems with a process that automatically achieves the classification of its phases via the computation of suitable metrics directly computable on a quantum processor. The operational pipeline is schematically depicted in Fig. 1. In a digital simulation scenario, the ground state of a system can be faithfully prepared on a processor [34, 35], on which observables, catching the critical behavior, are measured. Albeit it is a substantiated approach in model-targeted analog simulations, it falls short for digital ones and when little or no a priori information on the system under scrutiny is available. For such reason, we apply an agnostic metric that only relies on geometric aspects of the quantum states. Namely, we present an analysis of SVMs with fidelity kernels and we benchmark it to the broader class of tunable spin- $\frac{1}{2}$ chain in a magnetic field. Our analysis delves into the feasibility of the learning protocol and its resource scaling, we underline the impact of the broken symmetry in the shot requirements and kernel concentration.

II. THEORETICAL FRAMEWORK

In this section, we first introduce the Hamiltonian models for the critical quantum spin chains under investigation. Then we review the quantum kernel methods, based on fidelity and fidelity per site, that we are going to exploit for the classification of different phases and to identify the quantum phase transitions.

A. Anisotropic spin-1/2 models and symmetry structure

Since the early stages of quantum statistical mechanics, one-dimensional systems composed of interacting spins have served as paradigmatic models to study the emergence of complex structures in condensed matter. Due to their simple formulation and direct mapping of spin-1/2 degrees of freedom to qubits, they became pivotal testbeds for new techniques and the associated resource costs, especially in quantum machine learning [34, 36]. In the present work, we explore the suitability of fidelity-based support vector machines via a benchmark on spin-1/2 model with short range interaction, defined

by an anisotropic nearest-neighbor Hamiltonian

$$H = - \sum_{i=1}^N \left[\frac{1+\gamma}{2} \sigma_i^x \sigma_{i+1}^x + \frac{1-\gamma}{2} \sigma_i^y \sigma_{i+1}^y + \Delta \sigma_i^z \sigma_{i+1}^z \right] - h \sum_{i=1}^N \sigma_i^z, \quad (1)$$

having imposed PBC, such that $\sigma_{N+1} \equiv \sigma_1$ and with the Hamiltonian defined in units of a coupling constant J . This provides a unified description of several paradigmatic one-dimensional models upon tuning the anisotropy parameters, γ (for the xy plane) and Δ (for the longitudinal zz interaction), and the transverse field $h \geq 0$.

For $\Delta = 0$, one recovers the quantum XY chain, and the special points $\gamma = 1$ and $\gamma = 0$ correspond, respectively, to the quantum Ising chain and to the isotropic XX model. For $0 < \gamma \leq 1$, the model exhibits a continuous quantum phase transition in the Ising universality class between an ordered phase with nonvanishing magnetization along x and a quantum paramagnet at $h > h_c = 1$, where h_c is the critical field. In the ordered phase, the ground state is two-fold degenerate, reflecting the spontaneous breaking of a global spin-flip \mathbb{Z}_2 symmetry in the thermodynamic limit. However, for finite N the ground state is typically unique, with an exponentially small splitting between the lowest parity sectors, with an enhanced splitting due to translation symmetry for PBC. For $0 < \gamma \leq 1$, the model has only a discrete \mathbb{Z}_2 symmetry, while the continuous $U(1)$ symmetry is recovered only in the $\gamma = 0$ XX limit, where it admits a field-driven quantum phase transition separating a gapped paramagnetic phase in the region $h > 1$, from a gapless critical phase along all the region $h \leq 1$ [37].

For $\Delta \neq 0$ and $\gamma = 0$, the Hamiltonian reduces to the XXZ Heisenberg chain. In our sign convention, the zero-field phase diagram displays a gapless phase for $-1/2 < \Delta < 1/2$, separated by a Berezinskii–Kosterlitz–Thouless transition at $\Delta = -1/2$ from a gapped antiferromagnetic regime, while $\Delta = 1/2$ marks a first-order transition to the ferromagnetic phase.

The field term $-h \sum_i \sigma_i^z$ tunes the competition between the exchange couplings and the polarization along the z direction, and it is the control term used in the Ising/ XY / XX analyses discussed below. Its symmetry effect depends on the anisotropy sector: for $\gamma = 0$ (XX / XXZ), the Hamiltonian preserves the $U(1)$ symmetry associated with the conservation of S_{tot}^z . In this work, we do not attempt a complete finite-field phase diagram of Eq. (1). We rather focus on the field-driven transitions in the Ising/ XY / XX limits and on the zero-field XXZ transition structure relevant to our kernel analysis.

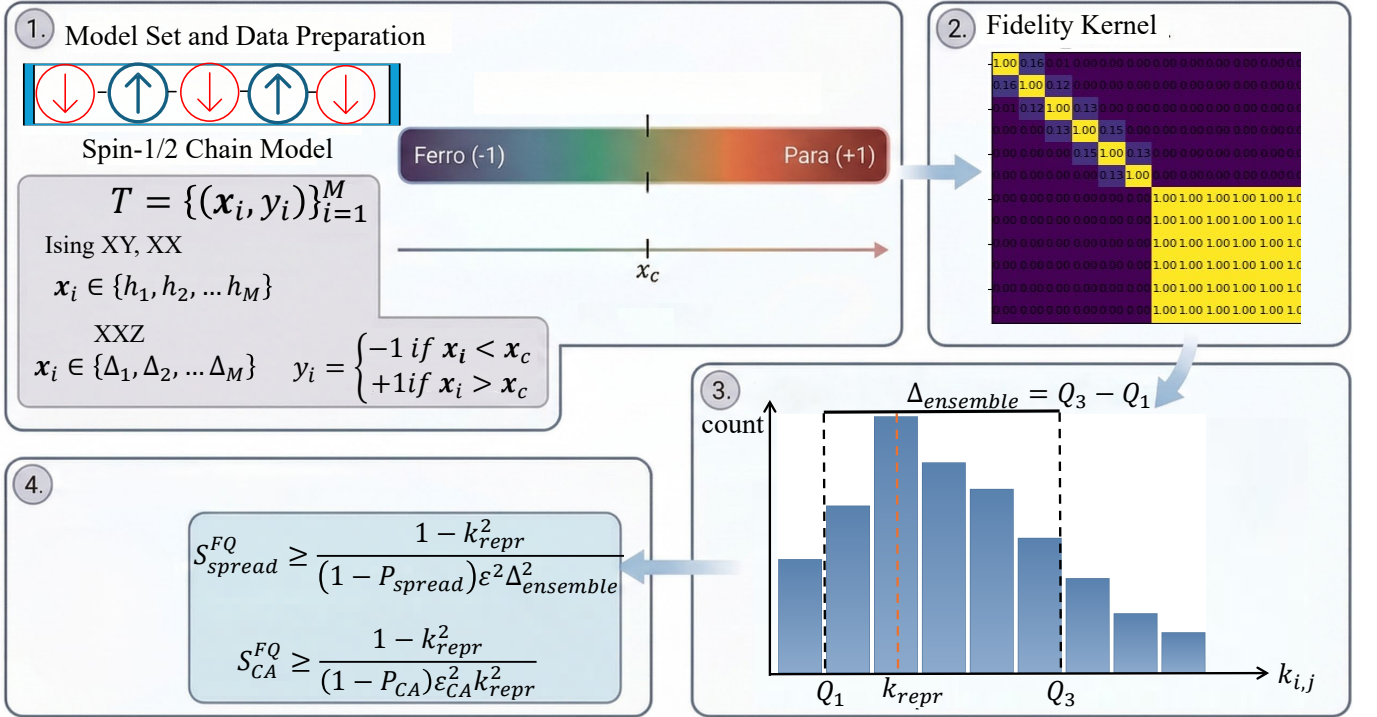


FIG. 1. Schematic overview of the quantum kernel estimation pipeline for many-body spin chain systems. **(1) Hamiltonian, phase labeling, and training set construction:** the anisotropic spin-chain Hamiltonian encompasses the Ising, XY, XX, XXZ models through the parameters (γ, Δ, h) . Training samples are chosen from two parameter windows on opposite sides of the critical point \mathbf{x}_c , assigning the labels $y_i = -1$ (ordered phase) and $y_i = +1$ (disordered phase). For the Ising universality class, the control parameter is $\mathbf{x}_i \equiv h_i$ while for XXZ it is $\mathbf{x}_i \equiv \Delta_i$. **(2) Fidelity kernel and Gram matrix:** the labeled samples are used to build the fidelity-based kernel matrix (Gram matrix) with entries $k_{i,j} = |\langle \psi(\mathbf{x}_i) | \psi(\mathbf{x}_j) \rangle|^2$, where $|\psi(\mathbf{x}_j)\rangle$ is the ground state for model parameters \mathbf{x}_j . **(3) Distribution of the elements of the Gram matrix:** the information about the phase transition is encoded in the entries of the Gram matrix. To visualize the distribution of the entries we can use a histogram of their values between 0 and 1. The median value is denoted as k_{repr} , and the spread of the distribution is quantified by the inter-quartile range (IQR) $\Delta_{ensemble} = Q_3 - Q_1$, where Q_1 and Q_3 are the first and third quartiles of the distribution. **(4) Finite-size resource bounds:** each fidelity $k_{i,j}$ may be estimated experimentally with a SWAP test. Given a finite number of experimental measurements, the estimated fidelity is subject to statistical fluctuations. The Chebyshev's inequality gives us a bound on the minimum number of measurements needed to ensure that the statistical fluctuations are small compared with the natural distribution of the Gram matrix elements.

B. SVM with fidelity kernels

Given training data $\{(\mathbf{x}_i, y_i)\}_{i=1}^M$ with $\mathbf{x}_i \in \mathbb{R}^d$ and labels $y_i \in \{-1, +1\}$, an SVM learns a maximum-margin separating hyperplane. The hard-margin primal problem can be written using the Lagrangian

$$\mathcal{L}(\mathbf{w}, b, \boldsymbol{\alpha}) = \frac{1}{2} \|\mathbf{w}\|^2 + \sum_{i=1}^M \alpha_i [1 - y_i(\mathbf{w}^\top \mathbf{x}_i + b)], \quad (2)$$

where α_i are Lagrange multipliers, $\mathbf{w} \in \mathbb{R}^d$ is the weight vector, and b is the bias. Stationarity with respect to \mathbf{w} and b implies $\mathbf{w} = \sum_{i=1}^M \alpha_i y_i \mathbf{x}_i$ and $\sum_{i=1}^M \alpha_i y_i = 0$. Substituting these conditions into \mathcal{L} yields a dual problem depending only on α ,

$$\mathcal{L}_D(\alpha) = \sum_i \alpha_i - \frac{1}{2} \sum_{i,j} \alpha_i \alpha_j y_i y_j \mathbf{x}_i^\top \mathbf{x}_j, \quad (3)$$

and this objective function must be maximized over $\alpha_i \geq 0$, subject to the constraint $\sum_i \alpha_i y_i = 0$. Typically, only a few α_i are non-zero, and the corresponding data points are known as support vectors. Therefore, the Lagrange multipliers α_i can be obtained by maximizing $\mathcal{L}_D(\alpha)$, and the support vectors allow for the estimation of the bias via $b = \frac{1}{|\text{SV}|} \sum_{k \in \text{SV}} (y_k - \sum_{i \in \text{SV}} \alpha_i y_i \mathbf{x}_i^\top \mathbf{x}_k)$, where SV denotes the set of support vectors, such that $\text{SV} = \{i \in \{1, \dots, M\} : \alpha_i > 0\}$, and $|\text{SV}|$ is the number of support vectors. While the formulation above describes a linear classifier, the true power of SVMs arises when the data are not linearly separable. In such cases, there may exist a map ϕ from the original input space to a higher-dimensional feature space, $\mathbf{x}_i \rightarrow \phi(\mathbf{x}_i)$, such that the data becomes linearly separable. A key advantage is that we do not need to compute this mapping explicitly, but we only need to evaluate inner products in the feature space, i.e. $\langle \phi(\mathbf{x}_i), \phi(\mathbf{x}_j) \rangle$, which can be computed through a kernel function $K(\mathbf{x}_i, \mathbf{x}_j)$. Replacing the inner product

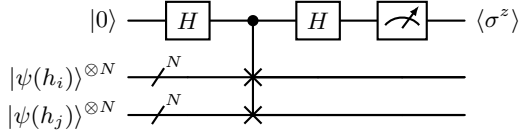


FIG. 2. Circuit diagram of the SWAP test employed to estimate the kernel entry $K(h_i, h_j) = |\langle \psi(h_i) | \psi(h_j) \rangle|^2$. An ancilla qubit controls N parallel SWAP gates, each acting on the corresponding pair of qubits from the two input registers. Measurement of the ancilla qubit yields the expectation value $\langle \sigma^z \rangle$, which is linearly related to the fidelity.

of the input space with a kernel function $K(\mathbf{x}_i, \mathbf{x}_j)$ yields

$$\mathcal{L}_D(\boldsymbol{\alpha}) = \sum_{i=1}^M \alpha_i - \frac{1}{2} \sum_{i,j=1}^M \alpha_i \alpha_j y_i y_j K(\mathbf{x}_i, \mathbf{x}_j). \quad (4)$$

A kernel $K(\mathbf{x}_i, \mathbf{x}_j)$ quantifies similarity between inputs. If K is symmetric and positive semidefinite, Mercer's theorem guarantees a feature map ϕ exists such that $K(\mathbf{x}_i, \mathbf{x}_j) = \langle \phi(\mathbf{x}_i), \phi(\mathbf{x}_j) \rangle$ [38]. Thus, evaluating K in input space is equivalent to computing an inner product in the (possibly high-dimensional) feature space.

In this work we employ a quantum-information-inspired similarity measure as the kernel. To this end, we introduce an inner product suited for the embedding of quantum many-body ground states. A natural choice is the Hilbert–Schmidt inner product, $\langle A, B \rangle_{\text{HS}} = \text{Tr}(A^\dagger B)$. We take the feature map to be the rank-one projector $\phi(\mathbf{x}) \equiv \rho(\mathbf{x}) = |\psi(\mathbf{x})\rangle \langle \psi(\mathbf{x})|$ on a \mathbf{x} -dependent wave function $|\psi(\mathbf{x})\rangle$, such that

$$K(\mathbf{x}_i, \mathbf{x}_j) = \langle \rho(\mathbf{x}_i), \rho(\mathbf{x}_j) \rangle_{\text{HS}} = \text{Tr}[\rho(\mathbf{x}_i)\rho(\mathbf{x}_j)]. \quad (5)$$

For pure states, this kernel reduces to the fidelity:

$$K(\mathbf{x}_i, \mathbf{x}_j) := |\langle \psi(\mathbf{x}_i) | \psi(\mathbf{x}_j) \rangle|^2. \quad (6)$$

By construction, the fidelity kernel is positive semidefinite and yields a symmetric positive-semidefinite (PSD) Gram matrix for any dataset. In the following, the model parameters serve as the data points, i.e. $\mathbf{x} = (h, \Delta, \gamma)$, that define the quantum feature map through the corresponding ground state $|\psi(\mathbf{x})\rangle$. The *signed decision* function is given by

$$d(\mathbf{x}) = \sum_{i=1}^M \alpha_i y_i K(\mathbf{x}_i, \mathbf{x}) + b, \quad (7)$$

where the sum is over the training data points. Here $d(\mathbf{x})$ is termed signed because it indicates the predicted class. If $d(\mathbf{x}) > 0$ the classifier predicts $\hat{y}(\mathbf{x}) = +1$, whereas if $d(\mathbf{x}) < 0$ it predicts $\hat{y}(\mathbf{x}) = -1$, i.e., $\hat{y}(\mathbf{x}) = \text{sign}(d(\mathbf{x}))$. The decision boundary is defined by the hyperplane $d(\mathbf{x}) = 0$. Furthermore, the magnitude $|d(\mathbf{x})|$ proportional to the distance from the hyperplane in feature space, serving as a measure of classification confidence.

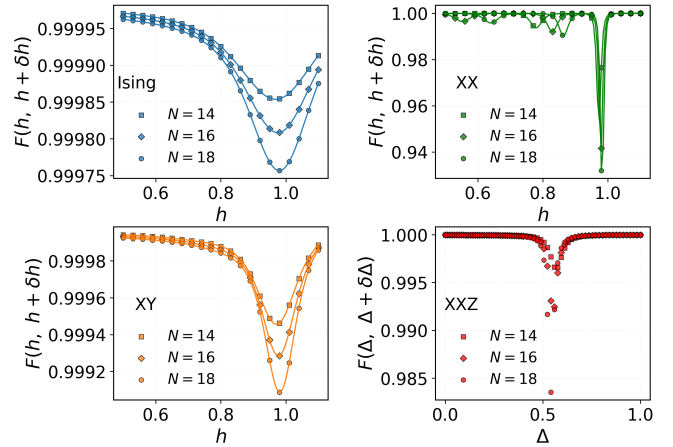


FIG. 3. Fidelity $F(\mathbf{x}, \mathbf{x} + \delta \mathbf{x})$ vs control parameter for $N = 14, 16, 18$. The dip marks the transition: near $h \approx 1$ for (Ising/XX/XY), and near $\Delta \approx 0.5$ for (XXZ, $h = 0$, first-order boundary). The BKT boundary at $\Delta \approx -0.5$ is analyzed in Appendix B.

We also consider an alternative kernel defined from the fidelity per site:

$$f_N(\mathbf{x}_i, \mathbf{x}_j) = [F(\mathbf{x}_i, \mathbf{x}_j)]^{1/N}. \quad (8)$$

Using the fidelity per site is sometimes a better choice as the fidelity may tend to decrease exponentially with increasing system size N [39]. This fidelity per site is also helpful when comparing different system sizes on the same scale.

C. SVM for quantum phase classification

The phase identification task can be viewed as a classification problem. In any realistic scenario involving systems with different phases, the target is to determine the critical points in the parameter space where the phase transitions occur. Due to finite resources, we may only estimate these points for finite system size N . We denote these finite-size pseudo-critical points as $h_c(N)$ and $\Delta_c(N)$, respectively. These pseudo-critical estimates are used to set the training windows on the two sides of the transition when constructing the labeled dataset (see Fig. 1). A well-known way to locate the phase transition is through the fidelity of nearby ground states [40–42], separated by a small parameter step $\delta \mathbf{x}$. We denote such a fidelity as $F(\mathbf{x}, \mathbf{x} + \delta \mathbf{x}) \equiv K(\mathbf{x}, \mathbf{x} + \delta \mathbf{x})$, where \mathbf{x} is the control parameter (either h or Δ in our settings). At the phase transition, such fidelity is expected to show a singular behavior. Figure 3 shows the nearest-neighbor fidelity $F(\mathbf{x}, \mathbf{x} + \delta \mathbf{x})$ as a function of the control parameter \mathbf{x} for several models and system sizes. In the Ising/XY/XX cases (panels a–c) we take $\mathbf{x} = h$, while for the XXZ chain at $h = 0$ (panel d) we take $\mathbf{x} = \Delta$. In all cases the transition region is signaled by a clear minimum of

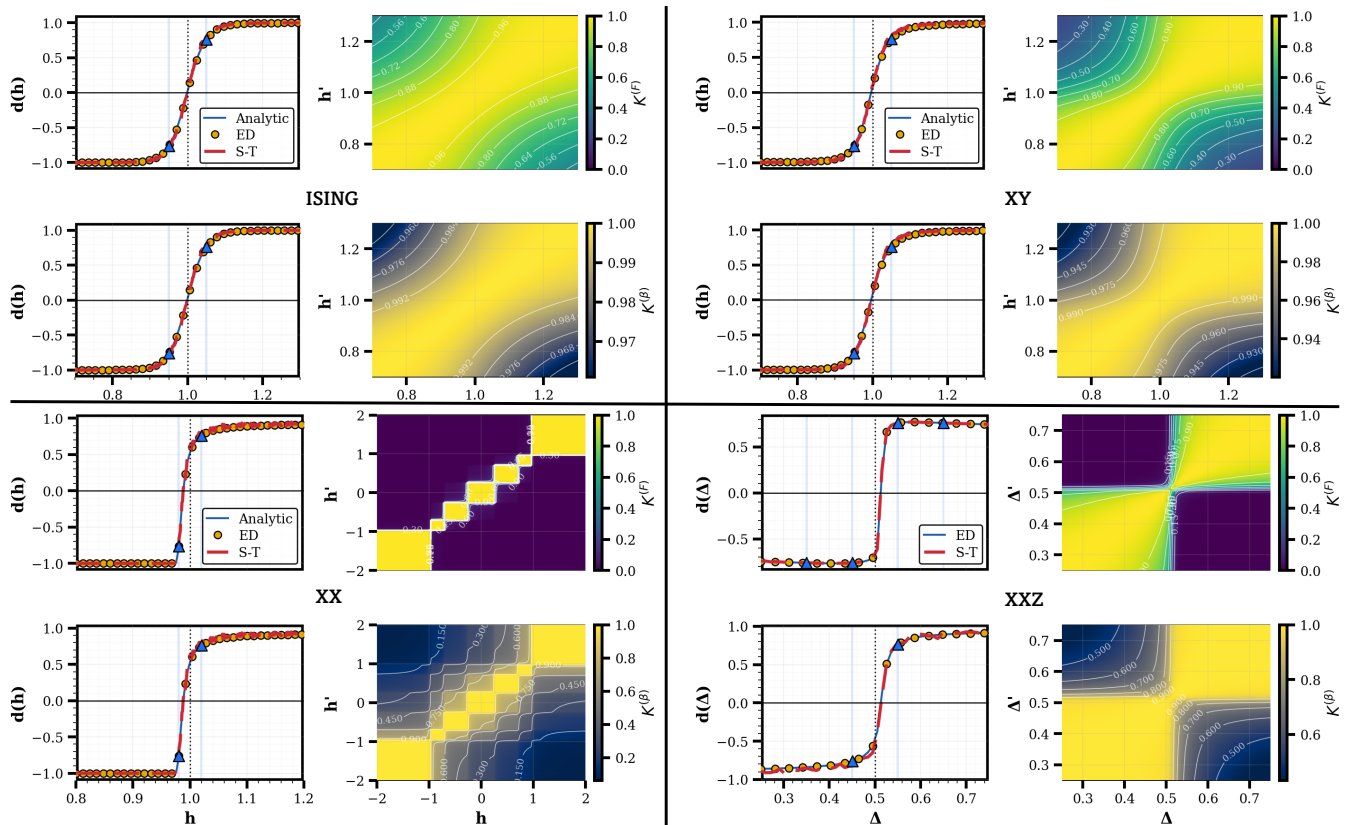


FIG. 4. The figure shows the signed SVM decision functions and the corresponding kernel matrices, for four Hamiltonian models. The signed SVM decision functions, introduced in Eq. (7), are shown in the line plots in the first and third columns. The kernel matrices are shown in the heat map plots in the second and fourth columns. In the decision-function panels, the horizontal axis is the control parameter (h for Ising/XY/XX, and Δ for XXZ), and the vertical axis is the signed decision function value $d(x)$. In the kernel-matrix panels, the horizontal and vertical axes label the pairwise control parameters used to build the Gram matrix (h, h' for Ising/XY/XX, and Δ, Δ' for XXZ), and the color scale gives the kernel value. SWAP-test (ST) estimates are benchmarked against numerical exact diagonalization (ED), and against the analytical result, when available (i.e. for the XY/XX cases). The vertical dotted line marks the expected critical point. For each model, the upper panels (first and third rows) show the kernel matrix defined from the global fidelity kernel, while the lower panels correspond to fidelity per site (see Eq. (8)). For the Ising/XY/XX panels, the SVM is trained on two field windows around the critical point $h_c = 1$, namely $h \in [0.7, 0.95] \cup [1.05, 1.3]$, using 16 training points per side ($M = 32$ total). For the XXZ panels (at $h = 0$), the SVM is trained on two anisotropy windows around the critical point $\Delta_c = 0.5$, namely $\Delta \in [0.35, 0.45] \cup [0.55, 0.65]$, using 16 training points per side ($M = 32$ total). For the XX case, we display the kernel matrix over a broad field range that includes both the gapless region ($h < 1$) and the saturated phase ($h > 1$), and we choose the training set from the same two windows around $h_c = 1$ as in the Ising/XY cases.

$F(\mathbf{x}, \mathbf{x} + \delta\mathbf{x})$, meaning that ground states separated by an infinitesimal parameter step become most distinguishable there.

The main objective of our work is to characterize SVM based on fidelity for the classification of quantum phase transitions. This implies estimating the kernel matrix, whose entries are the fidelities between ground states corresponding to different points in the training set. We emphasize that we chose such a quantum-information-informed kernel because it does not require any prior assumptions about order parameters or correlation functions. It offers a significant advantage for characterizing quantum phase transitions, but it is well known that its scalability can be challenging on actual devices. In case of the paradigmatic ferro/para-magnetic transition,

the signed decision function results in a powerful tool to quantitatively locate it [43]. Here we are extending this approach to gapless models such as XX and XXZ. For finite N , the position of this minimum defines a pseudo-critical estimate, whose shift with N captures finite-size corrections. Therefore, a rigorous analysis of resource scaling for systems of finite size is compelling to benchmark the usefulness of state-of-the-art quantum processors [35].

Before proceeding to the finite-size scaling analysis of the SVM estimates, it is useful to visualize the full output of the fidelity kernel framework for all models. Figure 4 reports the signed decision function $d(\mathbf{x})$ in Eq. (7) (left panels) and the corresponding Gram matrices (contour plots in the right panels). In the left panels we

also compare different methods to compute the kernel matrix: SWAP-test estimates, exact numerical diagonalization of the Hamiltonian, and, when available, the analytical form of the ground states. The vertical dotted line marks the expected critical points, where the decision function changes its sign, and the classifier switches phase labels. For each Hamiltonian model, the upper-right panels show the global fidelity kernel, whereas the lower-right panels show the fidelity-per-site kernel, introduced in Eq. (8). Notably, the decision function exhibits sharp behavior in the XX model for $h \leq 1$. Unlike other models with isolated critical points, the entire line ($\gamma = 0, h \leq 1$) is critical here. This manifests as a prominent central high-fidelity band displaying a distinctive staircase-like pattern.

III. FINITE-SIZE SCALING OF THE COMPUTATIONAL RESOURCES

The training of the SVM requires first to collect a training dataset of size M , and then to estimate the elements of the corresponding $M \times M$ Gram matrix, which, we recall is defined from the fidelity between different ground states. In an experimental setup the fidelity is estimated by exploiting the SWAP test, whose circuit diagram is depicted in Fig. 2. In the SWAP test, the probability P_0 of obtaining the outcome $|0\rangle$ when measuring the control qubit is related to the fidelity as

$$2P_0 - 1 = K(\mathbf{x}_i, \mathbf{x}_j). \quad (9)$$

However, for any finite number of runs of the circuit, one can only obtain the empirical relative frequency of outcome $|0\rangle$, from which the probability P_0 can only be estimated with a corresponding statistical error due to finite-size fluctuations.

In this section, we explore how the SVM performances depend on the choice and the size M of the training set, and on the number of repeated SWAP tests needed to estimate the fidelity. Both these quantities will depend on the size N of the given spin chain, and crucially on the symmetry of the considered Hamiltonian model.

A. Size and properties of the training set

In general, one would expect that increasing the size M of the training dataset will lead to improved accuracy in the determination of the critical point. Moreover, the way in which the training points are selected could affect the accuracy, for given size to the dataset.

We have investigated the relation between accuracy and the properties and size of the training dataset, for the four Hamiltonian models under our investigation. We have considered equally spaced training data points chosen within an interval centered around the transition point. As a general trend, as it should be expected, we find that increasing the number of M training points leads

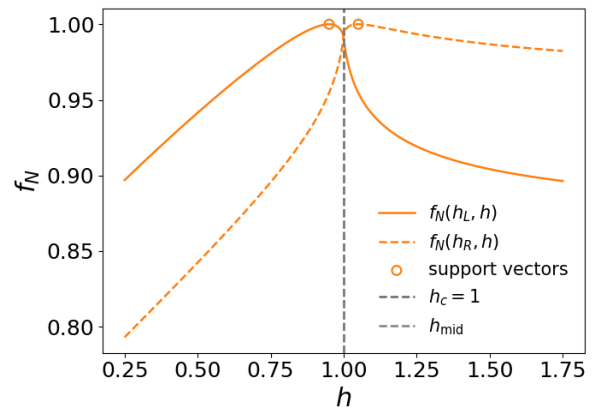


FIG. 5. Decision boundary as a geometric midpoint for the per-site fidelity kernel (XY chain, $\gamma = 0.5$). We train an SVM with a precomputed per-site kernel $f_N(h, h') = F(h, h')^{1/N}$ on two field windows $h \in [0.76, 0.95] \cup [1.05, 1.30]$ (16 points per side, $M = 32$ total), using the analytical Bogoliubov-angle fidelity at $N = 1000$. The solid and dashed curves show the similarities to the *inner* (dominant) support vectors, plotted as $f_N(h_L, h)$ and $f_N(h_R, h)$, where $h_L = \max\{h_i : \alpha_i > 0, y_i = -1\}$ and $h_R = \min\{h_i : \alpha_i > 0, y_i = +1\}$. Open circles mark the two dominant support vectors. The dashed vertical line marks the expected critical field $h_c = 1$, while the dotted line marks the midpoint estimate h_{mid} defined by $f_N(h_L, h_{\text{mid}}) = f_N(h_R, h_{\text{mid}})$.

to higher accuracy. This is shown in Fig. 6. A similar trend is obtained using randomly chosen training data points within the same interval. In both cases, we observe that models with increasing symmetry (we recall that the symmetry increases when moving from Ising to XY and to XX models) require a larger training data set to achieve comparable accuracy in the determination of the estimated transition point.

To achieve a better understanding of the relation between accuracy and the size M of the training dataset, we need to investigate where the SVM places the separating hyperplane. This is related to the support vectors. Here we focus on the *dominant* support vectors, which are defined as those support vectors that mainly determine the boundary: i.e. either they correspond to points closest to the critical region in parameter space, or those with the largest α_i (or both). Then we consider the case where there are two dominant vectors: one from the left interval and one from the right interval around the true critical point \mathbf{x}_c , denoted as \mathbf{x}_L and \mathbf{x}_R , respectively. Also, we denote as α_L and α_R the corresponding nonzero dual coefficients, and the corresponding ground states are $|\psi(\mathbf{x}_L)\rangle$ and $|\psi(\mathbf{x}_R)\rangle$. Their mutual distance is [44]

$$\begin{aligned} D(\mathbf{x}_L, \mathbf{x}_R) &= \|\phi(\mathbf{x}_L) - \phi(\mathbf{x}_R)\| \\ &= \sqrt{K(\mathbf{x}_L, \mathbf{x}_L) + K(\mathbf{x}_R, \mathbf{x}_R) - 2K(\mathbf{x}_L, \mathbf{x}_R)} \\ &= \sqrt{2(1 - K(\mathbf{x}_L, \mathbf{x}_R))}, \end{aligned} \quad (10)$$

where the last step uses the normalization $K(\mathbf{x}, \mathbf{x}) = 1$

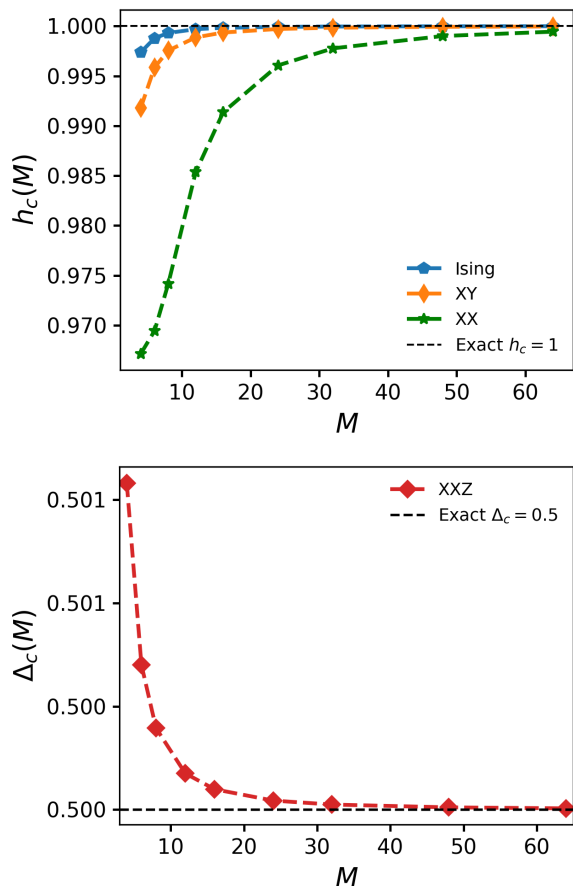


FIG. 6. SVM estimates of the critical point versus the training-set size M . The upper panel is for the Ising model ($\gamma = 1$, $\Delta = 0$), the XY model ($\gamma = 0.5$, $\Delta = 0$), and the XX model ($\gamma = 10^{-3}$, $\Delta = 0$), for $N = 12$ sites. For these models we have chosen M training points equally spaced within the interval $h \in [0.85, 1.15]$, which is centered around the transition point $h_c = 1$. The lower panel is for the XXZ model ($\gamma = 10^{-3}$, $h = 0$). For this model we have chosen M training points equally spaced within the interval $\Delta \in [0.35, 0.65]$, which is centered around the transition point $\Delta_c = 0.5$. The black dashed lines mark the exact critical values ($h_c = 1$ in the upper panel and $\Delta_c = 0.5$ in the lower panel).

induced by the fidelity. To determine the exact location of the decision boundary, we recall the dual constraint of the SVM optimization $\sum_i \alpha_i y_i = 0$. In our symmetric scenario with two dominant support vectors with labels, $y_L = -1$, $y_R = +1$, this constraint implies $\alpha_L = \alpha_R$. Consequently, in this symmetric idealized case the bias term vanishes ($b \simeq 0$), and the separating hyperplane is placed exactly at the geometric midpoint where the fidelities to the support vectors are balanced, namely $D(\mathbf{x}_L, \mathbf{x}) = D(\mathbf{x}_R, \mathbf{x})$. In Fig. 5 the two curves show, for the XY model, the kernel similarities to dominant support vectors, plotted as $f_N(h_L, h)$ and $f_N(h_R, h)$. The decision boundary corresponds to the geometric midpoint between $\phi(h_L)$ and $\phi(h_R)$, i.e., the point h_{mid} where the

similarities balance, $f_N(h_L, h_{\text{mid}}) = f_N(h_R, h_{\text{mid}})$ (vertical dotted line), which is equivalent to equal distances $\|\phi(h_L) - \phi(h_{\text{mid}})\| = \|\phi(h_R) - \phi(h_{\text{mid}})\|$.

As a consequence of that, training near the critical value yields a better estimation of the zero-crossing of the decision function (discussed in Eq. (7)). As shown in Fig. 6, for a fixed training interval, the SVM estimate of the critical point starts to settle as we increase the number of training points M . This is physically intuitive: when we have very few points, the SVM does not have enough information to capture what happens close to the transition, so the estimated boundary can shift. As we add more points, the SVM eventually identifies the most important ones, i.e., the support vectors.

What matters in our construction is that the training set is sampled from two fixed parameter windows placed on opposite sides of the transition. Denote these windows as $I_L = [\mathbf{x}_L^{\min}, \mathbf{x}_L^{\max}]$ and $I_R = [\mathbf{x}_R^{\min}, \mathbf{x}_R^{\max}]$, with $\mathbf{x}_L^{\max} < \mathbf{x}_R^{\min}$. The endpoints are therefore the four boundary values $\mathbf{x}_L^{\min}, \mathbf{x}_L^{\max}, \mathbf{x}_R^{\min}, \mathbf{x}_R^{\max}$, which are known once the windows are chosen. The two values closest to the critical region are the *inner endpoints*, \mathbf{x}_L^{\max} and \mathbf{x}_R^{\min} , and they *bracket* the transition in parameter space in the sense that the true critical point satisfies $\mathbf{x}_L^{\max} < \mathbf{x}_c < \mathbf{x}_R^{\min}$. Importantly, we do not know the support vectors a priori. The SVM identifies them during training as the samples with nonzero dual coefficients $\alpha_i > 0$ that constrain the maximum-margin solution. In this one-dimensional and approximately symmetric setup, the inner endpoints ($\mathbf{x}_L^{\max}, \mathbf{x}_R^{\min}$) are often selected among the dominant support vectors because they provide the tightest constraints near the transition. Once these constraints are present, adding more samples strictly inside the same intervals typically yields $\alpha_i = 0$ for the additional points and does not change the separating hyperplane, so the estimated boundary saturates. Saturation tends to occur faster for models with discrete \mathbb{Z}_2 symmetry (Ising and XY) than for those with continuous $U(1)$ symmetry (XX and XXZ).

B. Sample complexity for the estimation of the Gram matrix

Here we focus on assessing the relation between the accuracy in the estimation of the kernel and the number of repeated SWAP tests (referred to as measurement shots).

Recently, Miroszewski *et al.* have provided a bound to estimate the minimum number of shots needed to reliably resolve the spread of kernel values in a quantum kernel setting [45]. The present work extends this framework in three directions. First, we adapt the shot bounds from a ZZ feature-map kernel to fidelity-based kernels estimated via the SWAP test. Second, through an analytical calculation of the Bogoliubov-angle sensitivity (Eq. (16)), we establish a direct quantitative connection between the symmetry class of the model and the degree of kernel con-

centration, explaining the shot-cost hierarchy $\text{Ising} < \text{XY} < \text{XX}$ from first principles. Third, we extend the analysis to the genuinely interacting XXZ-model and demonstrate that the enhanced $SU(2)$ symmetry near the isotropic point¹ further amplifies the resource cost beyond the free-fermion $U(1)$ case.

As discussed in Sec. IIB, in a general quantum kernel estimation scenario, each kernel entry $k_{i,j} = K(\mathbf{x}_i, \mathbf{x}_j)$ is accessed through the SWAP test and estimated from a finite number of shots, denoted S . In the ℓ -th measurement shot, the ancillary qubit is measured in the computational basis, yielding a binary outcome $z_\ell \in \{0, 1\}$, where $z_\ell = 1$ corresponds to the outcome $|0\rangle$, and vice versa. The empirical estimator of the probability is then constructed as

$$\hat{P}_0 = \frac{1}{S} \sum_{\ell=1}^S z_\ell, \quad (11)$$

from which one obtains the estimate for the kernel entry as per Eq. (9). The estimated entry $\hat{k}_{i,j}$ is a random variable that fluctuates across independent runs, as it is obtained from a finite number of shots S in the SWAP test. The natural reference quantity is therefore its mean value $\mathbb{E}[\hat{k}_{i,j}]$, which in the noiseless case coincides with the ideal kernel entry $k_{i,j}$. In practice, whenever an exact ground-truth value is available (e.g., from exact diagonalization, or from the analytical formula in the free-fermion XY/XX limits), we use that value as a benchmark for the SWAP-test estimate. Hence, for one entry, we quantify the measurement error as the absolute deviation from the mean, or in the benchmarks from the ground-truth value, as $|\hat{k}_{i,j} - \mathbb{E}[\hat{k}_{i,j}]|$.

The key point is that, in a kernel method, what matters is not only that each entry is estimated, but that the overall structure of the Gram matrix is well preserved despite statistical fluctuations. If the typical fluctuations $|\hat{k}_{i,j} - \mathbb{E}[\hat{k}_{i,j}]|$ become comparable to the typical variation of kernel values across the dataset, then different entries become hardly distinguishable, and the Gram matrix is effectively blurred. However, checking the separation $|k_{i,j} - k_{p,q}|$ for all possible pairs of entries in an $M \times M$ Gram matrix is not practical. Therefore, it is convenient to introduce a single quantity that represents the overall spread of the kernel. Following Ref. [45], we consider the interquartile range (IQR)

$$\Delta_{\text{ensemble}} = \text{IQR}(k) = Q_3 - Q_1, \quad (12)$$

where Q_1, Q_3 are the quartile, which captures the middle 50% of the kernel values and is less sensitive to outliers than the full range. We then impose a resolution requirement such that the shot-noise deviation of each estimated

entry should be smaller than a fraction ε of this ensemble spread, namely $|\hat{k}_{i,j} - \mathbb{E}[\hat{k}_{i,j}]| < \varepsilon \Delta_{\text{ensemble}}$. We require this to hold with confidence level P_{spread} , i.e.

$$\Pr\left(|\hat{k}_{i,j} - \mathbb{E}[\hat{k}_{i,j}]| \geq \varepsilon \Delta_{\text{ensemble}}\right) \leq 1 - P_{\text{spread}}. \quad (13)$$

Using Chebyshev's inequality and $\text{Var}(\hat{k}_{i,j}) = (1 - k_{i,j}^2)/S$ for the SWAP-test estimator, we obtain the spread-effect shot bound

$$S_{\text{spread}} \geq \frac{1 - k_{\text{repr}}^2}{(1 - P_{\text{spread}}) \varepsilon^2 \Delta_{\text{ensemble}}^2}. \quad (14)$$

This expression makes the scaling law transparent: the required number of shots scales as $1/\varepsilon^2$ (stricter tolerance) and as $1/\Delta_{\text{ensemble}}^2$ (kernel concentration). In particular, when the kernel values concentrate, i.e. for small Δ_{ensemble} , even a small absolute sampling $|\hat{k}_{i,j} - \mathbb{E}[\hat{k}_{i,j}]|$ noise can wash out the relative differences between entries, and the required shot count can grow rapidly. Considering any real situation, the true $k_{i,j}$ value for each pair is unknown or unfeasible to obtain. Therefore, for resource estimation, we replace it with a representative value k_{repr} . In our noiseless benchmark, we obtain k_{repr} as the median of the upper-triangular kernel entries computed via exact diagonalization (ED), and we estimate Δ_{ensemble} from the quartiles. Thus, S_{spread} quantifies how many shots are needed to resolve the *spread* of kernel values across the dataset.

It is also useful to estimate the shot cost to avoid the concentration of the estimator around zero. Using again $\text{Var}(\hat{k}_{i,j}) = (1 - k_{i,j}^2)/S$ for the SWAP-test estimator, and replacing $k_{i,j}$ by the representative value k_{repr} (as above), the concentration-avoidance (CA) bound reads

$$S_{\text{CA}} \geq \frac{1 - k_{\text{repr}}^2}{(1 - P_{\text{CA}}) \varepsilon_{\text{CA}}^2 k_{\text{repr}}^2}, \quad (15)$$

where P_{CA} is the confidence level and ε_{CA} is the tolerance.

IV. RESULTS

In this section, we discuss the results of our resource-estimation analysis and report the main numerical findings. We compare the bounds on the number of measurement shots across the four models under study, and highlight how the required measurement resources scale with the system size and with the choice of control parameter.

A. Free-fermion XY family

In Fig. 7(a), we report the required number of shots S_{spread} to estimate the kernel entries $\hat{k}_{i,j}$ within the spread criterion. We observe that S_{spread} can be very

¹ At the isotropic point $\Delta = \frac{1}{2}$ the model matches with the Heisenberg model that possesses $SU(2)$ symmetry.

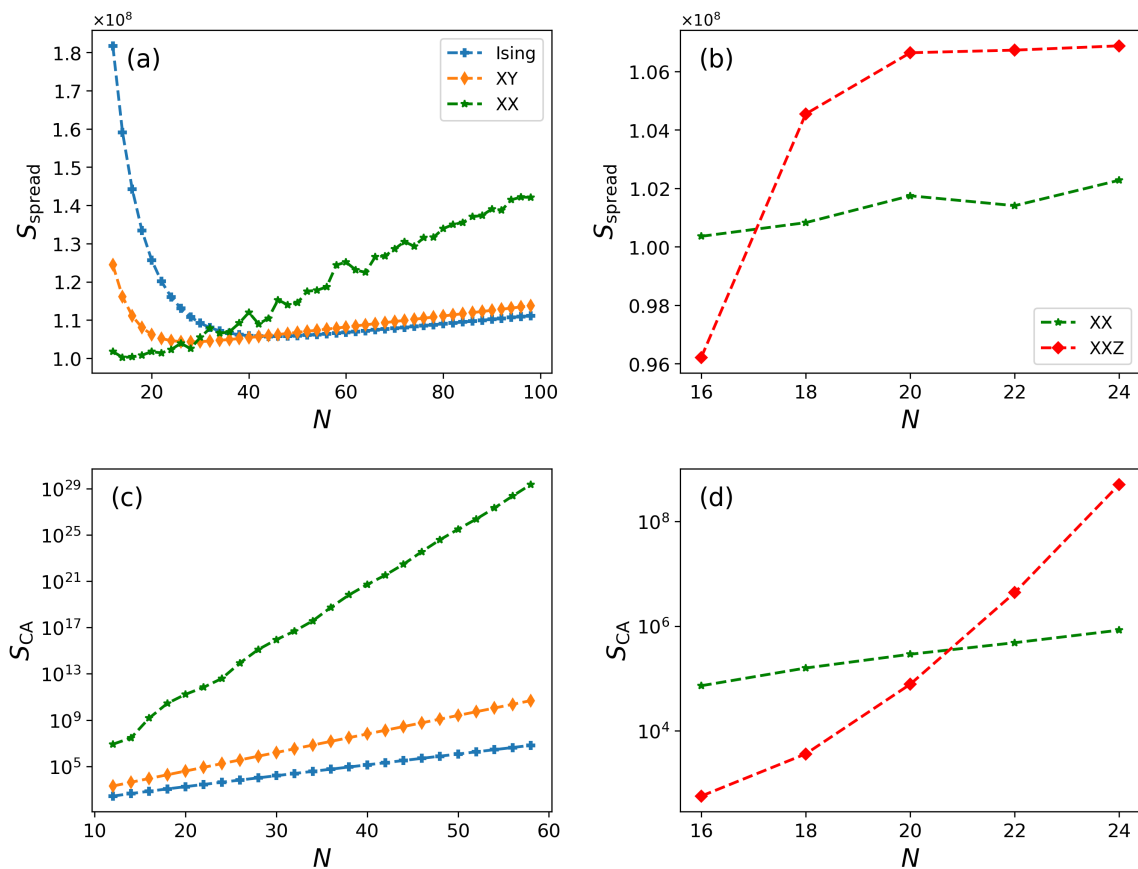


FIG. 7. Finite-size bounds on the number of measurement shots needed to estimate the fidelity-based quantum kernels via the SWAP test. The number of measurement shots is evaluated using the spread bound in Eq. (14), obtaining the estimate S_{spread} , and the concentration-avoidance bound in Eq. (15), yielding the estimate S_{CA} . The training windows are the same as in Fig. 4: for Ising/XY/XX we sample $h \in [0.7, 0.95] \cup [1.05, 1.3]$ at $\Delta = 0$ (Ising $\gamma = 1$, XY $\gamma = 0.5$, XX $\gamma = 10^{-3}$), while for XXZ we sample $\Delta \in [0.35, 0.45] \cup [0.55, 0.65]$ at $h = 0$ and $\gamma = 10^{-3}$. (a) S_{spread} versus N for the free-fermion XY family (Ising/XY/XX). (b) S_{spread} comparison between XX and XXZ for $N = 16-24$. (c) S_{CA} versus N for the XY family (log scale). (d) S_{CA} comparison between XX and XXZ for $N = 16-24$ (log scale). These finite-size estimates are obtained by putting $\varepsilon = 10^{-3}$, $P_{\text{spread}} = 0.99$, $\varepsilon_{\text{CA}} = 10^{-3}$, and $P_{\text{CA}} = 0.99$.

large for small system sizes, which we mainly attribute to finite-size effects: for small N the kernel ensemble does not yet display a stable separation between the two parameter regions used in the training set. As N increases, ground states taken from opposite sides of the transition become progressively more distinguishable, since their overlaps decrease, and the kernel distribution becomes more spread out. As a result, the bound predicts a reduction in the required number of shots up to an intermediate size. Interestingly, for larger N the required shots increase again. This non-monotonic behavior is due to a concentration of many off-diagonal kernel values near zero, which reduces the ensemble spread Δ_{ensemble} . Since the bound requires $|\hat{k}_{i,j} - \mathbb{E}[\hat{k}_{i,j}]| < \varepsilon \Delta_{\text{ensemble}}$, a smaller Δ_{ensemble} implies a larger number of shots, scaling as $S_{\text{spread}} \propto 1/\Delta_{\text{ensemble}}^2$. We also find that reducing the anisotropy parameter γ (i.e. by passing from Ising to XY, and then to the XX limit) significantly increases the resource cost. This hierarchy (Ising $<$ XY $<$ XX) is

driven by the sensitivity of the ground state wavefunction to parameter changes. To understand the origin of this behavior, we compute the rate at which the ground state rotates in Hilbert space. The ground state is determined by the Bogoliubov angles $\theta_q(h) = \frac{1}{2} \arctan w_q$, with $w_q = \frac{\gamma \sin q}{h - \cos q}$ (see Appendix A for more details). Applying the chain rule $\partial_h \theta_q = \frac{1}{2} \frac{1}{1+w_q^2} \frac{\partial w_q}{\partial h}$, we find:

$$\begin{aligned} \frac{\partial \theta_q}{\partial h} &= \frac{1}{2} \frac{(h - \cos q)^2}{(h - \cos q)^2 + \gamma^2 \sin^2 q} \left[\frac{-\gamma \sin q}{(h - \cos q)^2} \right] \\ &= -\frac{1}{2} \frac{\gamma \sin q}{E_q^2}, \end{aligned} \quad (16)$$

where $E_q^2 = (h - \cos q)^2 + \gamma^2 \sin^2 q$ is the squared energy gap and q is momentum mode. Eq. (16) reveals that the wavefunction sensitivity is inversely proportional to the square of the energy gap, scaled by the anisotropy γ . This allows us to analyze the impact of symmetry case

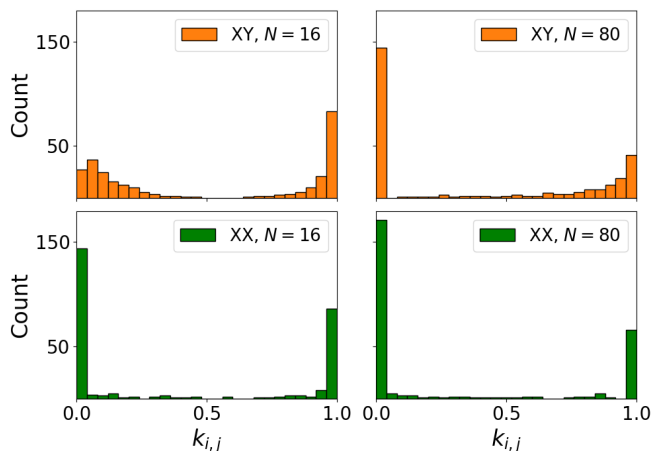


FIG. 8. Histogram of the fidelity-kernel entries $k_{i,j}$ (upper-triangular part) for the XY and XX models at two system sizes. The left column shows $N = 16$ (top: XY, bottom: XX), while the right column shows $N = 80$ (top: XY, bottom:XX).

by case:

(i) *Ising Limit* ($\gamma = 1$): The model has a discrete \mathbb{Z}_2 symmetry. Away from h_c the gap is finite, so $|\partial_h \theta_q|$ stays bounded and the kernel ensemble retains a larger spread, leading to a lower shot cost.

(ii) *XY Model* ($\gamma = 0.5$): The symmetry is still \mathbb{Z}_2 , preserving a finite gap. However, the pre-factor in the derivative scales as $1/\gamma$. Reducing γ from 1 to 0.5 effectively doubles the sensitivity of the wavefunction. This sharper response leads to faster orthogonality decay compared to the Ising case, explaining the consistently higher resource requirement.

(iii) *XX Limit* ($\gamma \rightarrow 0$): This regime represents a fundamental change in the universality class. As $\gamma \rightarrow 0$, the Hamiltonian restores a continuous $U(1)$ rotation symmetry. This forces the energy gap to close ($E_q \rightarrow 0$ at the critical momentum defined by $h - \cos q_c = 0$). Inspecting Eq. (16) at resonance ($h \approx \cos q$), the derivative diverges as:

$$\left| \frac{\partial \theta_q}{\partial h} \right| \approx \frac{1}{2\gamma \sin q} \rightarrow \infty. \quad (17)$$

This implies that for the gapless $U(1)$ phase, even infinitesimal parameter perturbations cause a macroscopic rotation of the ground state. This leads to the kernel values concentrating near zero so rapidly that the cost rises monotonically for all observed $N \geq 16$, lacking the non-monotonic minimum seen in case of Ising and XY. This mechanism is further illustrated in Fig. 8. Since kernel entries concentrate near zero in this regime, it is useful to focus on the CA-type shot requirement in Eq. (15), in order to avoid such concentration. Accordingly, Fig. 7(c) reports the number of shots needed to avoid concentration. When the kernel values concentrate near zero ($k_{\text{repr}} \rightarrow 0$), the required number of shots blows up since $S_{\text{CA}} \propto 1/k_{\text{repr}}^2$.

B. XXZ chain

We treated the XXZ case separately because, unlike the XY family, we do not have access to a simple closed-form analytical expression for the ground-state wave function in the interacting regime. Therefore, we rely on exact numerical diagonalization,

$$|\psi(\Delta)\rangle = \arg \min_{\|v\|=1} \langle v | H(\Delta) | v \rangle. \quad (18)$$

In the XXZ limit ($\gamma = 0$) at zero field ($h = 0$), the model exhibits critical points at $\Delta = \pm 1/2$. $\Delta = -1/2$ corresponds to a Berezinskii–Kosterlitz–Thouless (BKT) transition, while $\Delta = +1/2$ marks the ferromagnetic boundary². Here we focus on the ferromagnetic transition, and accordingly we train the SVM in parameter windows around $\Delta = 1/2$. By contrast, the BKT transition $\Delta = -1/2$ is notoriously hard to detect from finite-size data and kernel-based features. This is discussed in more detail in Appendix B.

Figure 7(b) compares the XXZ chain with the XX model for system sizes $N = 16, \dots, 24$, around the $\Delta = 1/2$ transition. Within the XY family, the XX regime already shows the largest measurement shot cost. Here we observe that the interacting XXZ model requires even more shots according to the spread bound. This trend is consistent with Fig. 7(d): once N is large enough, such that finite-size effects are reduced, the number of shots for the XXZ chain is larger than for the XX model within the same N range. Due to limited computational resources, we restrict to $N \leq 24$, but we expect this separation to persist at larger system sizes.

A natural interpretation is that, unlike the XY chains, the XXZ model is genuinely interacting. Interaction modifies the distribution of kernel entries and can reduce the ensemble spread, thereby increasing S_{spread} . Concerning symmetries, the XX chain has a $U(1)$ symmetry. By contrast, the XXZ chain becomes fully $SU(2)$ -symmetric at the isotropic point $\Delta = 1/2$ for $h = 0$.

In terms of our resource bounds, the $SU(2)$ symmetry tends to reshape the distribution of kernel entries by increasing concentration and reducing the effective spread Δ_{ensemble} (and driving k_{repr} toward smaller values), which directly amplifies both S_{spread} and S_{CA} through Eqs. (14) and (15). This effect is absent in the free-fermion XX chain, where the $U(1)$ symmetry is present but the ground-state manifold is simpler and admits a non interacting description.

² These values for the critical points follows from our sign convention in Eq. (1). Note that this differs from the more common notation found in literature [46–50], where the critical values are $\tilde{\Delta} = \pm 1$. The relation with our notation is $\Delta = -\tilde{\Delta}/2$.

V. CONCLUSION AND OUTLOOK

We have established a direct link between many-body symmetries and the measurement overhead of quantum kernel estimation, revealing that continuous symmetries systematically increase shot requirements through kernel concentration. This symmetry-resource hierarchy \mathbb{Z}_2 (Ising/XY) \ll U(1) (XX) $<$ SU(2)-approaching (XXZ) emerges, as shown both analytically and numerically, persisting beyond finite-size effects. It allowed us to tackle the phase transition of finite order with good accuracy when benchmarked with ground-truth values.

The following three implications are given. First, symmetry exploitation in quantum-informed ML is double-edged: while continuous symmetries simplify ground states analytically, they paradoxically degrade kernel discriminability on NISQ hardware. Second, our concentration-avoidance bound $S_{CA} \propto 1/k_{\text{repr}}^2$, as in Eq. (15), and provides a practical diagnostic for when fidelity kernels fail, favoring discrete-symmetry models for early quantum advantage. Third, the observed non-monotonic shot scaling (minimum $\sim N = 30$) suggests optimal system sizes for balancing distinguishability against concentration.

Looking ahead, our paper paves the way for the extensions to the analysis of systems in higher-dimensional lattices for which analytical methods are not available. Our symmetry-resource framework establishes a new benchmark for investigating critical systems on digital quantum simulators, in the spirit of physics-informed quantum algorithms. Our shot bounds enable precise resource accounting for fidelity-kernel estimation on near-term QPUs, prioritizing \mathbb{Z}_2 -symmetric models (Ising/XY) over U(1)/SU(2) cases for scalable phase recognition. Extensions to higher-dimensional lattices and physics-informed kernel mitigation, such as regularization, adaptive collocation sampling, will unlock digital quantum simula-

tion of regimes fundamentally inaccessible to commonly employed analytical tools, ultimately allowing us to explore new phases of matter on early fault-tolerant hardware. When finalizing the manuscript, we noted [51], in which the authors report a quantum algorithm enabling an efficient estimation of fidelity susceptibility overcoming classical exponential scaling limitations. They have shown that for frustration-free Hamiltonians, a quadratic speedup further enhances efficiency. This aligns seamlessly with our work, reinforcing scalable quantum digital approaches to critical systems.

ACKNOWLEDGMENTS

This work has received funding from the European Union — Next Generation EU through PNRR MUR Project No. CN00000013, “Italian National Centre on HPC, Big Data and Quantum Computing” and PNRR MUR Project No. PE0000023-NQSTI, “National Quantum Science and Technology Institute”; and INFN through the project “QUANTUM.” AM acknowledges the IRA Programme, project no. FENG.02.01-IP.05-0006/23, financed by the FENG program 2021-2027, Priority FENG.02, Measure FENG.02.01., with the support of the FNP.

DATA AND CODE AVAILABILITY

All results reported in this work are based on *synthetic* data generated numerically. No experimental datasets were used. The code used to generate the synthetic states, compute the labels and features, train the machine-learning models, and reproduce all figures and numerical results will be shared by the corresponding author upon reasonable request.

-
- [1] S. Sachdev, *Quantum Phase Transitions*, 2nd ed. (Cambridge University Press, Cambridge, 2011).
 - [2] T. Giamarchi, *Quantum Physics in One Dimension* (Oxford University Press, Oxford, 2004).
 - [3] L. Amico, R. Fazio, A. Osterloh, and V. Vedral, Entanglement in many-body systems, *Reviews of Modern Physics* **80**, 517 (2008).
 - [4] X.-G. Wen, Colloquium: Zoo of quantum-topological phases of matter, *Reviews of Modern Physics* **89**, 041004 (2017).
 - [5] J. I. Latorre and A. Riera, A short review on entanglement in quantum spin systems, *Journal of Physics A: Mathematical and Theoretical* **42**, 504002 (2009).
 - [6] H. Bethe, Zur theorie der metalle: I. eigenwerte und eigenfunktionen der linearen atomkette, *Zeitschrift für Physik* **71**, 205 (1931).
 - [7] P. Pfeuty, The one-dimensional ising model with a transverse field, *Ann. Phys.* **57**, 79 (1970).
 - [8] G. Vidal, J. I. Latorre, E. Rico, and A. Kitaev, Entanglement in quantum critical phenomena, *Phys. Rev. Lett.* **90**, 227902 (2003).
 - [9] I. Affleck, T. Kennedy, E. H. Lieb, and H. Tasaki, Rigorous results on valence-bond ground states in antiferromagnets, *Phys. Rev. Lett.* **59**, 799 (1987).
 - [10] I. Bloch, J. Dalibard, and W. Zwerger, Many-body physics with ultracold gases, *Rev. Mod. Phys.* **80**, 885 (2008).
 - [11] A. Browaeys and T. Lahaye, Many-body physics with individually controlled rydberg atoms, *Nature Physics* **16**, 132 (2020).
 - [12] X. Zhang, C.-L. Hung, S.-K. Tung, and C. Chin, Observation of quantum criticality with ultracold atoms in optical lattices, *Science* **335**, 1070 (2012).
 - [13] P. Gegenwart, Q. Si, and F. Steglich, Quantum criticality in heavy-fermion metals, *Nature Physics* **4**, 186 (2008).
 - [14] R. Coldea, D. A. Tennant, E. M. Wheeler, E. Wawrzynska, D. Prabhakaran, M. Telling, K. Habicht, P. Smeibidl,

- and K. Kiefer, Quantum criticality in an ising chain: experimental evidence for emergent e_8 symmetry, *Science* **327**, 177 (2010).
- [15] P. Huembeli, A. Dauphin, and P. Wittek, Identifying quantum phase transitions with adversarial neural networks, *Phys. Rev. B* **97**, 134109 (2018).
- [16] K. Ch'ng, J. Carrasquilla, R. G. Melko, and E. Khatami, Machine learning phases of strongly correlated fermions, *Phys. Rev. X* **7**, 031038 (2017).
- [17] D.-L. Deng, X. Li, and S. Das Sarma, Machine learning topological states, *Phys. Rev. B* **96**, 195145 (2017).
- [18] A. Canabarro, F. F. Fanchini, A. L. Malvezzi, R. Pereira, and R. Chaves, Unveiling phase transitions with machine learning, *Phys. Rev. B* **100**, 045129 (2019).
- [19] J. Carrasquilla and R. G. Melko, Machine learning phases of matter, *Nature Physics* **13**, 431 (2017).
- [20] V. Kasatkin, E. Mozgunov, N. Ezzell, and D. Lidar, Detecting quantum and classical phase transitions via unsupervised machine learning of the fisher information metric, arXiv <https://doi.org/10.48550/arXiv.2408.03418> (2024), arXiv:2408.03418.
- [21] L. Wang, Discovering phase transitions with unsupervised learning, *Phys. Rev. B* **94**, 195105 (2016).
- [22] S. J. Wetzell, Unsupervised learning of phase transitions: From principal component analysis to variational autoencoders, *Phys. Rev. E* **96**, 022140 (2017).
- [23] E. P. L. van Nieuwenburg, Y.-H. Liu, and S. D. Huber, Learning phase transitions by confusion, *Nat. Phys.* **13**, 435 (2017).
- [24] C. Giannetti, B. Lucini, and D. Vadacchino, Machine learning as a universal tool for quantitative investigations of phase transitions, *Nuclear Physics B* **944**, 114639 (2019).
- [25] R. Mengoni and A. Di Pierro, Kernel methods in quantum machine learning, *Quantum Machine Intelligence* **1**, 65 – 71 (2019).
- [26] T. Sancho-Lorente, G. García-Pérez, and D. Zueco, Quantum kernels to learn the phases of quantum matter, *Physical Review A* **105**, 042432 (2022).
- [27] Y. Wu, J. Sun, Z. Zhao, D. Wang, J. Zavatone-Veth, N. Yu, P. Rebentrost, J. M. Taylor, J. Vučković, H.-Y. Huang, *et al.*, Quantum phase recognition via quantum kernel methods, *Quantum* **7**, 981 (2023).
- [28] Y. Wang and L. Cao, Quantum phase transition detection via quantum support vector machine, *Quantum Science and Technology* **10**, 015043 (2025).
- [29] M. Schuld and N. Killoran, Quantum machine learning in feature hilbert spaces, *Phys. Rev. Lett.* **122**, 040504 (2019).
- [30] Y. Liu, S. Arunachalam, and K. Temme, A rigorous and robust quantum speed-up in supervised machine learning, *Nat. Phys.* **17**, 1013 (2021).
- [31] H.-Y. Huang, M. Broughton, M. Mohseni, R. Babbush, S. Boixo, H. Neven, and J. R. McClean, Power of data in quantum machine learning, *Nat. Commun.* **12**, 2631 (2021).
- [32] V. Havlíček, A. D. Córcoles, K. Temme, A. W. Harrow, A. Kandala, J. M. Chow, and J. M. Gambetta, Supervised learning with quantum-enhanced feature spaces, *Nature* **567**, 209 (2019).
- [33] S. Thanasilp, H. Yamasaki, B. Regula, V. Kendon, M. Muraio, *et al.*, Exponential concentration in quantum kernel methods, *Nat. Commun.* **15**, 49287 (2024).
- [34] M. Grossi, O. Kiss, F. De Luca, C. Zollo, I. Gremese, and A. Mandarino, Finite-size criticality in fully connected spin models on superconducting quantum hardware, *Phys. Rev. E* **107**, 024113 (2023).
- [35] O. Kiss, D. Teplitskiy, M. Grossi, and A. Mandarino, Statistics of topological defects across a phase transition in a digital superconducting quantum processor, *Quantum Science and Technology* **10**, 10.1088/2058-9565/addf75 (2025).
- [36] F. P. Barone, O. Kiss, M. Grossi, S. Vallecorsa, and A. Mandarino, Counterdiabatic optimized driving in quantum phase sensitive models, *New Journal of Physics* **26**, 033031 (2024).
- [37] F. Franchini, *An Introduction to Integrable Techniques for One-Dimensional Quantum Systems* (Springer International Publishing, 2017).
- [38] B. Schölkopf and A. J. Smola, *Learning with kernels: support vector machines, regularization, optimization, and beyond* (MIT press, 2002).
- [39] S.-J. Gu, Fidelity approach to quantum phase transitions, *Int. J. Mod. Phys. B* **24**, 4371 (2010).
- [40] P. Zanardi and N. Paunković, Ground state overlap and quantum phase transitions, *Phys. Rev. E* **74**, 031123 (2006).
- [41] L. Campos Venuti and P. Zanardi, Quantum critical scaling of the geometric tensors, *Phys. Rev. Lett.* **99**, 095701 (2007).
- [42] P. Zanardi, M. Cozzini, and P. Giorda, Ground state fidelity and quantum phase transitions in free Fermi systems, *Journal of Statistical Mechanics: Theory and Experiment* **2007**, L02002–L02002 (2007).
- [43] C. Giannetti, B. Lucini, and D. Vadacchino, Machine learning as a universal tool for quantitative investigations of phase transitions, *Nuclear Physics B* **944**, 114639 (2019).
- [44] B. Schölkopf, The kernel trick for distances, *Advances in Neural Information Processing Systems* (2001).
- [45] A. Miroszewski, M. F. Asiani, J. Mielczarek, B. L. Saux, and J. Nalepa, In search of quantum advantage: Estimating the number of shots in quantum kernel methods, arXiv <https://doi.org/10.48550/arXiv.2407.15776> (2024), arXiv:2407.15776.
- [46] T. Giamarchi, *Quantum Physics in One Dimension* (Clarendon Press, Oxford, 2004).
- [47] D. C. Cabra and P. Pujol, Field-theoretical methods in quantum magnetism, in *Quantum Magnetism*, Lecture Notes in Physics, Vol. 645, edited by U. Schollwöck, J. Richter, D. J. J. Farnell, and R. F. Bishop (Springer, Berlin, Heidelberg, 2004) pp. 253–305.
- [48] H.-J. Mikeska and A. K. Kolezhuk, One-dimensional magnetism, in *Quantum Magnetism*, Lecture Notes in Physics, Vol. 645, edited by U. Schollwöck, J. Richter, D. J. J. Farnell, and R. F. Bishop (Springer, Berlin, Heidelberg, 2004) pp. 1–83.
- [49] B. Wang, M. Feng, and Z.-Q. Chen, Berezinskii-Kosterlitz-Thouless transition uncovered by the fidelity susceptibility in the XXZ model, *Physical Review A* **81**, 064301 (2010).
- [50] S. Pradhan, J. Cobos, E. Rico, and G. Sierra, Oddities in the entanglement scaling of the quantum six-vertex model, arXiv preprint <https://doi.org/10.1103/wvng-2vyb> (2025), arXiv:2502.19152 [cond-mat.str-el].
- [51] Y. Zhang and X. Yuan, Quantum algorithms for fidelity susceptibility: From quantum criticality to metrology,

Phys. Rev. Lett. **136**, 080604 (2026).

- [52] M. E. Fisher and M. N. Barber, Scaling theory for finite-size effects in the critical region, Physical review letters **28**, 1516 (1972).
- [53] Z. Sun, L. Wang, P. Zanardi, and F. C. Zhang, Fidelity at Berezinskii–Kosterlitz–Thouless quantum phase transitions, Phys. Rev. B **91**, 014418 (2015), arXiv:1408.2739.
- [54] L. Cincio, M. M. Rams, J. Dziarmaga, and W. H. Zurek, Universal shift of the fidelity susceptibility peak away from the critical point of the Berezinskii–Kosterlitz–Thouless quantum phase transition, Phys. Rev. B **100**, 081108(R) (2019), arXiv:1906.05307.
- [55] Y.-C. Tzeng, H.-Q. Ding, C.-Y. Mou, and M.-F. Yang, Fidelity approach to gaussian transitions, Phys. Rev. A **77**, 062321 (2008), arXiv:0804.0537.
- [56] H.-K. Tang, M. A. Marashli, and W. C. Yu, Novel approach to unveil quantum phase transitions using fidelity map, arXiv <https://doi.org/10.48550/arXiv.2104.13845> (2021), arXiv:2104.13845.
- [57] B. Wang, M. Feng, and Z.-Q. Chen, Berezinskii–Kosterlitz–Thouless transition uncovered by the fidelity susceptibility in the xxz model, Phys. Rev. A **81**, 064301 (2010).
- [58] H.-L. Wang, H.-H. Zhao, J.-P. Zhang, and H.-D. Li, Kosterlitz–Thouless phase transition and ground state fidelity: a novel perspective from matrix product states, J. Stat. Mech. , L10001 (2011).
- [59] J. M. Kosterlitz, Kosterlitz–thouless physics: a review of key issues, Reports on Progress in Physics **79**, 026001 (2016).
- [60] Y.-D. Hsieh, Y.-J. Kao, and A. W. Sandvik, Finite-size scaling method for the Berezinskii–Kosterlitz–Thouless transition, Journal of Statistical Mechanics: Theory and Experiment , P09001 (2013).
- [61] U. Schollwöck, The density-matrix renormalization group, Rev. Mod. Phys. **77**, 259 (2005).

Appendix A: Bogoliubov-angle fidelity for the transverse-field XY chain

For completeness, we briefly review the standard diagonalization of the transverse-field XY chain and derive the closed-form expression for the ground-state fidelity used in the main text.

We consider the transverse-field XY model with periodic boundary conditions,

$$H(\gamma, h) = - \sum_{j=1}^N \left(\frac{1+\gamma}{2} \sigma_j^x \sigma_{j+1}^x + \frac{1-\gamma}{2} \sigma_j^y \sigma_{j+1}^y \right) - h \sum_{j=1}^N \sigma_j^z, \quad (\text{A1})$$

Under the Jordan–Wigner transformation, the spin Hamiltonian becomes quadratic in fermionic operators up to a boundary term whose sign depends on the fermion-parity sector. In the finite-size analysis considered here, we work in the even-parity sector, which leads to antiperiodic boundary conditions for the fermions. The transform-

ation reads

$$\sigma_j^+ = c_j^\dagger \prod_{\ell=1}^{j-1} (-\sigma_\ell^z), \quad \sigma_j^- = \left(\prod_{\ell=1}^{j-1} (-\sigma_\ell^z) \right) c_j, \\ \sigma_j^z = 1 - 2c_j^\dagger c_j, \quad (\text{A2})$$

Eq. (A1) becomes (up to an additive constant)

$$H(\gamma, h) = - \sum_{j=1}^N \left(c_j^\dagger c_{j+1} + c_{j+1}^\dagger c_j + \gamma c_j^\dagger c_{j+1}^\dagger + \gamma c_{j+1} c_j \right) + 2h \sum_{j=1}^N c_j^\dagger c_j. \quad (\text{A3})$$

Let $N_f = \sum_j c_j^\dagger c_j$ be the fermion-number operator and $P = (-1)^{N_f}$ the fermion-parity operator. Restricting to the even-parity sector, $P = +1$, implies antiperiodic boundary conditions $c_{N+1} = -c_1$, and therefore the allowed momenta are

$$q = \frac{(2m+1)\pi}{N}, \quad m = 0, 1, \dots, \frac{N}{2} - 1. \quad (\text{A4})$$

Using $c_j = \frac{1}{\sqrt{N}} \sum_q e^{iqj} c_q$, the Hamiltonian decouples into independent $(q, -q)$ sectors,

$$H(\gamma, h) = \sum_{q>0} H_q + \text{const}, \quad (\text{A5})$$

with

$$H_q = 2\epsilon_q (c_q^\dagger c_q + c_{-q}^\dagger c_{-q}) + 2i\Delta_q (c_q^\dagger c_{-q}^\dagger - c_{-q} c_q), \quad (\text{A6})$$

where

$$\epsilon_q := h - \cos q, \quad \Delta_q := \gamma \sin q. \quad (\text{A7})$$

The first term is diagonal in the occupation basis whereas the second term is not yet diagonal and this motivates the Bogoliubov transformation

$$\eta_q = u_q c_q - i v_q c_{-q}^\dagger \quad \eta_{-q} = u_q c_{-q} + i v_q c_q^\dagger \quad (\text{A8})$$

A convenient choice is $u_q = \cos \theta_q$, $v_q = \sin \theta_q$ for which H_q is diagonal provided

$$\tan(2\theta_q(h)) = \frac{\Delta_q}{\epsilon_q} = \frac{\gamma \sin q}{h - \cos q}. \quad (\text{A9})$$

With this choice,

$$H_q = 2\varepsilon_q (\eta_q^\dagger \eta_q + \eta_{-q}^\dagger \eta_{-q} - 1), \quad (\text{A10})$$

Where dispersion is

$$\varepsilon_q = \sqrt{\epsilon_q^2 + \Delta_q^2} = \sqrt{(h - \cos q)^2 + \gamma^2 \sin^2 q}. \quad (\text{A11})$$

This yields a closed-form expression for the Bogoliubov angle. A convenient explicit choice consistent with Eq. (A9) is

$$\theta_q(h) = \frac{1}{2} \arctan\left(\frac{\gamma \sin q}{h - \cos q}\right) \quad (\text{A12})$$

Because the ground state factorizes over $q > 0$, the fidelity between two ground states at fields h_a and h_b (same γ) factorizes mode by mode as

$$F(h_a, h_b) := |\langle \psi(h_a) | \psi(h_b) \rangle|^2 = \prod_{q>0} \cos^2(\theta_q(h_b) - \theta_q(h_a)). \quad (\text{A13})$$

In Eq. (A13), q runs over the even-parity momenta in Eq. (A4), and $\theta_q(h)$ is given by Eq. (A12). Equation (A13) is the analytical expression used in the main text to construct both the global fidelity kernel in Eq. (6) and the fidelity-per-site kernel in Eq. (8).

We further use this closed-form fidelity to compare SVM-based pseudo-critical estimates with a training-free benchmark. For the latter, we define

$$h_c^{(\text{bench})}(N) = \arg \max_h \left| \partial_h \mathcal{S}(h, h_{\text{ref}}) \right|, \quad (\text{A14})$$

where $\mathcal{S}(h, h_{\text{ref}})$ denotes a similarity measure built either from the global fidelity, Eq. (6), or from the fidelity per site, Eq. (8), with h_{ref} a fixed reference field in the paramagnetic regime far from the critical point. To extrapolate the finite-size pseudo-critical points, we use the empirical drift form [52]

$$h_c(N) = h_c + a N^{-p}, \quad (\text{A15})$$

where p denotes an effective finite-size drift exponent and together with a , is treating as a fitting parameter. The resulting fits are shown in Fig. 9 and summarized in Table A.

Appendix B: Remarks on the BKT transition in the XXZ chain

It is an open question in the literature whether the fidelity susceptibility is a universally reliable detector of quantum phase transitions in particular, for BKT-type transitions it may remain non-divergent and, even when it exhibits a dip, the location of the minimum can be shifted away from the true critical point, so minima-based localization can be misleading at finite size [53–56]. On the other hand, several works show that fidelity-based indicators can still reveal BKT transitions provided one employs an appropriate finite-size scaling analysis, or improved fidelity-based constructions, with explicit demonstrations in XXZ-type settings [39, 56–58].

Consistently, in our analysis we find that the BKT transition is detectable within a fidelity-based approach, but the finite-size convergence is extremely slow. This is

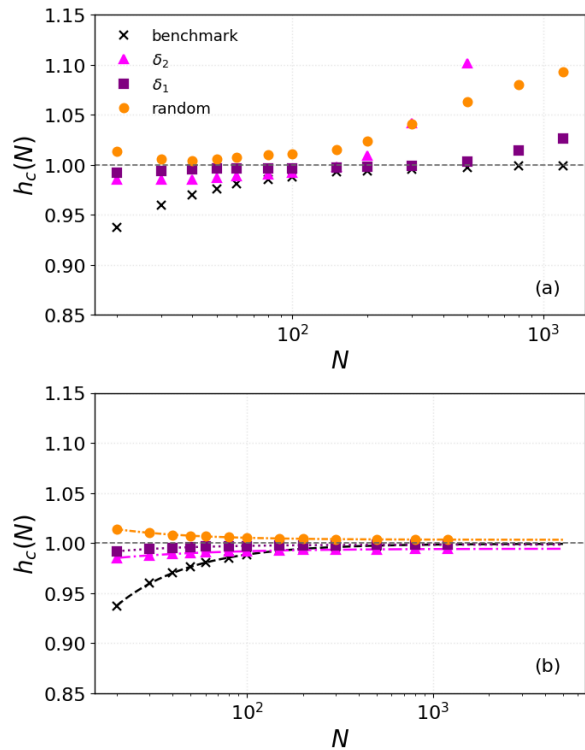


FIG. 9. Finite-size scaling of the pseudo-critical field in the XY chain ($\gamma = 0.5$). For each system size N (log scale on the horizontal axis), we extract a pseudo-critical point $h_c(N)$ using: (i) a training-free benchmark (black \times), with $h_{\text{ref}} = 1.75$; and (ii) an SVM decision-boundary estimate $d(h) = 0$ trained on $M = 16$ labeled points (8 per phase) with three sampling strategies: $\delta_1 = [0.85, 0.90] \cup [1.10, 1.15]$ (purple squares), $\delta_2 = [0.60, 0.70] \cup [1.60, 1.70]$ (magenta triangles), and random uniform sampling in $[0.25, 1.75]$ labeled according to the sign of $h - 1$ (yellow circles). *Top panel*: SVM trained with the global fidelity kernel, Eq. (6). *Bottom panel*: SVM trained with the fidelity-per-site kernel, Eq. (8). The horizontal dotted line marks the thermodynamic critical value $h_c = 1$. The dashed and dotted curves are fits showing the convergence of $h_c(N)$ with increasing N .

consistent with the BKT form of the correlation-length divergence [59],

$$\xi(\Delta) \sim \xi_0 \exp\left(\frac{c}{\sqrt{|\Delta - \Delta_c|}}\right), \quad (\text{B1})$$

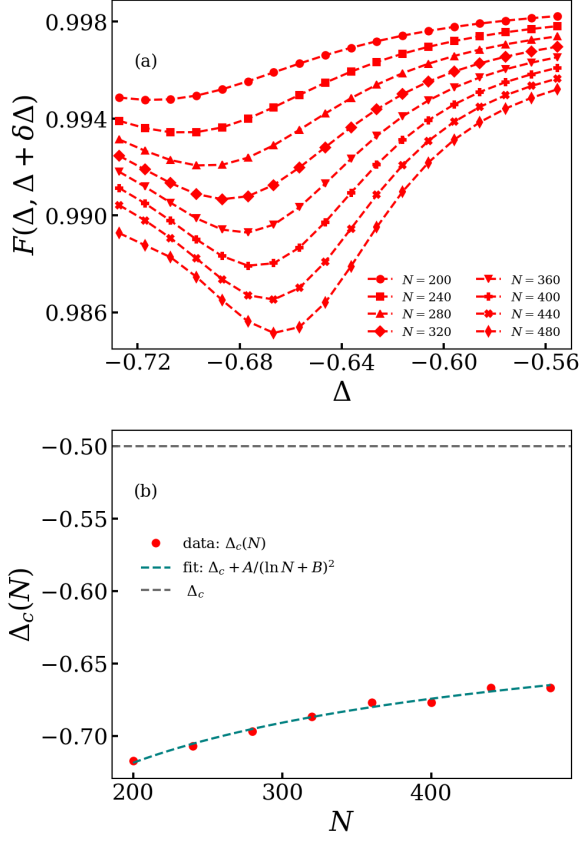
where ξ is the correlation length, ξ_0 is a nonuniversal microscopic scale, and $c > 0$ is a nonuniversal constant. In practice, Eq. (B1) implies that pseudo-critical estimators drift toward Δ_c only very slowly with system size. By setting $\xi(\Delta_c(N)) \sim N$ in Eq. (B1), taking the logarithm, and squaring yields Eq. (B2).

$$\Delta_c(N) = \Delta_c + \frac{A}{(\ln N + B)^2}, \quad (\text{B2})$$

where A and B are fit parameters. We fit the observed drift with the (B2). Accordingly, the fidelity-kernel SVM

Method	h_c	p	a
benchmark	0.999339 ± 0.000544	0.945 ± 0.126	$-1.458 \times 10^0 \pm 9.092 \times 10^{-1}$
δ_2	0.994163 ± 0.000020	1.170 ± 0.022	$-1.304 \times 10^{-1} \pm 8.883 \times 10^{-3}$
δ_1	0.998629 ± 0.000011	1.469 ± 0.020	$-3.834 \times 10^{-2} \pm 1.451 \times 10^{-3}$
random	1.002729 ± 0.000009	1.292 ± 0.010	$8.741 \times 10^{-2} \pm 2.203 \times 10^{-3}$

TABLE I. Finite-size scaling fit of the empirical drift form $h_c(N) = h_c + aN^{-p}$ for the pseudo-critical points extracted from the benchmark and SVM-based estimators. Reported values are best-fit parameters $\pm 1\sigma$.



can also detect the transition, but the classifier boundary converges very slowly and requires larger system sizes N to stabilize [60]. Using Density Matrix Renormalization Group (DMRG) [61], we estimate the pseudo-critical points $\Delta_c(N)$ up to $N = 480$ (see Fig. 10) and extrapolate the data, obtaining $\Delta_c^{\text{obtained}} \approx -0.5201$, which is close to the expected critical value $\Delta_c = -0.5$.

FIG. 10. (a) Ground-state fidelity $F(\Delta, \Delta + \delta\Delta)$ as a function of the control parameter Δ for system sizes $N = 200$ – 480 , computed with $\delta\Delta = 0.005$. (b) Finite-size drift of the pseudo-critical points $\Delta_c(N)$ extracted from the fidelity data and their extrapolation.